A&A, 710, A78 (2026)
https://doi.org/10.1051/0004-6361/202558085

Astronomy & Astrophysics

Helium-induced rotational (de-)excitation of interstellar rhomboidal silicon tricarbide (*c*-SiC_3)

Bilel Mehnen*

Institute of Physics, Faculty of Physics, Astronomy and Informatics, Nicolaus Copernicus University in Toruń, Grudziądzka 5, 87-100 Toruń, Poland

Received 12 November 2025 / Accepted 7 April 2026

ABSTRACT

Silicon carbide molecules are key tracers of dust formation and molecular evolution in carbon-rich circumstellar environments, yet their collisional excitation remains largely unexplored. We report the first quantum scattering study of the collisional (de-)excitation of interstellar rhomboidal silicon tricarbide (*c*-SiC_3) by helium atoms under low-temperature conditions relevant to astrophysical environments. We computed a high-accuracy 3D potential energy surface (3D-PES) for the *c*-SiC_3 – He interaction at the CCSD(T)-F12a/aug-cc-pVTZ level of theory and analytically represented in terms of spherical harmonics. The global minimum of the PES lies at a T-shaped configuration with a well depth of about 42 cm^{-1}, revealing a highly anisotropic interaction. State-to-state inelastic cross-sections were computed using the close-coupling formalism for total energies up to 400 cm^{-1}. The corresponding thermal rate coefficients were evaluated for kinetic temperatures between 5 and 50 K and found to display a strong propensity for even Δj transitions, dominated by $\Delta j = \pm 2$ transitions induced by the V_{20} anisotropic term. These data represent the first set of collisional rate coefficients for *c*-SiC_3 and provide essential input for nonlocal thermodynamic equilibrium (NLTE) radiative transfer models. They are crucial for interpreting observed line emission transitions in carbon-rich circumstellar envelopes such as IRC+10216 and offer valuable guidance for future searches for silicon-carbon ring species in the interstellar medium.

Key words. ISM: abundances – molecular data – molecular processes – scattering – methods: numerical

1. Introduction

Carbon-chain molecules play a central role in interstellar chemistry, contributing substantially to the molecular diversity of the interstellar medium (ISM) across environments ranging from cold dark clouds to the envelopes of evolved stars. These species are valuable tracers of physical and chemical conditions in space due to their high stability, large dipole moments, and strong rotational transitions. Pure carbon clusters, including C_2, C_3, and C_5 (Souza & Lutz 1977; Hinkle et al. 1988; Bernath et al. 1989), have been identified in both diffuse clouds and circumstellar envelopes, confirming the remarkable resilience of carbon-based species in the gas phase.

The incorporation of heteroatoms such as hydrogen, oxygen, sulfur, nitrogen, phosphorus, and metals further expands the chemical diversity of carbon-chain species. Among these, carbon-chain radicals such as the hydrocarbons C_nH (n = 2–5) (Tucker et al. 1974; Guélin et al. 1978; Gottlieb et al. 1983; Thaddeus et al. 1985; Mangum & Wootten 1990; Cabezas et al. 2022; McGuire 2022) are particularly abundant in sources such as TMC-1 and in photon-dominated regions, highlighting the efficiency of gas-phase reactions linking radicals, ions, and neutral molecules. Oxygen-terminated carbon chains such as C_2O and C_3O (Brown et al. 1985, 1991; Ohishi et al. 1991), as well as their sulfur analogs C_nS (n = 2–5) (Saito et al. 1987; Yamamoto et al. 1987; Bell et al. 1993; Cernicharo et al. 2021), emphasize the important role of these elements in interstellar chemistry. Nitrogen-bearing carbon chains, including C_3N and the cyanopolyynes HC_nN (n = 3−11) (Broten et al. 1978; Kawaguchi et al. 1992a,b; Cernicharo et al. 2020; Loomis et al. 2021), are especially abundant and serve as key tracers of nitrogen chemistry in dense molecular environments.

Metal–carbon containing molecules form another important subclass. Magnesium- and silicon-bearing species such as MgCN, MgNC, MgC_3N, SiC, SiCN, and SiNC (Cernicharo et al. 1989; Kawaguchi et al. 1993; Guélin et al. 2000, 2004; Cernicharo et al. 2019; Pardo et al. 2021) illustrate how metals can stabilize reactive carbon frameworks at low temperatures. In particular, silicon plays a prominent role in carbon chemistry, especially in the carbon-rich envelopes of evolved stars. The detection of *c*-SiC_2 in IRC+10216 (Thaddeus et al. 1984) was the first identification of a cyclic molecule in space, followed by longer homologues SiC_3 and SiC_5 (Cernicharo et al. 2025), along with related species such as SiCSi (Cernicharo et al. 2015).

Subsequent laboratory measurements led to the detection of five new linear silicon carbides: SiC_3, SiC_5, SiC_6, SiC_7, and SiC_8 (McCarthy et al. 2000; Pardo et al. 2025). These discoveries highlight silicon's ability to promote bonding diversity and stabilize bent, linear, or cyclic carbon frameworks under astrophysical conditions. Rhomboidal silicon tricarbide (*c*-SiC_3) represents a particularly intriguing member of this family. Identified toward IRC+10216 through seven millimeter-wave transitions (Apponi et al. 1999), *c*-SiC_3 is a planar, highly polar ($\mu \sim 4.2$ D), and rigid rhomboidal ring molecule. Its rotational excitation pattern shows two distinct regimes: intra-K-stack transitions corresponding to low rotational temperatures (∼10−20 K) and inter-K transitions exhibiting higher excitation temperatures (∼50 K), corresponding to the local kinetic temperature of the circumstellar shell. The derived column density,

* Corresponding author: bilel.mehnen20@gmail.com

$N(SiC_3) \sim 4.3 \times 10^{12}\,cm^{-2}$, indicates that c-SiC_3 may be more abundant than its linear precursor SiC_4, in contrast to photochemical model predictions (Howe & Millar 1990). These conditions suggest the presence of alternative formation pathways, possibly involving direct reactions between silicon-bearing precursors and carbon clusters.

Despite its astrophysical relevance, no quantum scattering data currently exist for collisions of c-SiC_3 with major interstellar colliders such as He or H_2. The lack of such data limits the accuracy of nonlocal thermodynamic equilibrium (NLTE) radiative transfer modeling and, consequently, the reliability of abundance determinations. Given its large dipole moment, optically thin emission, and well-characterized laboratory spectrum, c-SiC_3 represents an ideal candidate for detailed collisional studies. Accurate state-to-state rate coefficients are essential for interpreting current observations and guiding future searches for silicon-carbon species in both interstellar and circumstellar environments. In this work, we present the first quantum scattering calculations for the rotational excitation and de-excitation of interstellar c-SiC_3 induced by collisions with helium atoms. The resulting state-to-state rate coefficients, computed over a range of astrophysically relevant temperatures, provide the first quantitative collisional data for this species. These results offer a foundation for reliable NLTE modeling of c-SiC_3 emission and contribute to a deeper understanding of silicon-carbon chemistry in carbon-rich environments such as IRC +10216.

2. Molecular structure and rotational spectroscopy of rhomboidal c-SiC_3

Rhomboidal c-SiC_3, a cyclic isomer of silicon tricarbide, represents the global minimum on the PES for the SiC_3 molecular system, as established by high-level ab initio calculations (Alberts et al. 1990; Linguerri et al. 2006). This molecule adopts a planar, rhomboidal geometry in its electronic ground state ($^1A_1$), characterized by a four-membered ring comprising three carbon atoms and one silicon atom, with a transannular Si − C bond that stabilizes the structure. The planarity and symmetry of the molecule result in a C_{2v} point group, and the bonding framework is consistent with delocalized π-character across the ring. Isotopic substitution experiments, conducted through laboratory microwave spectroscopy, have enabled accurate determination of molecular bond lengths and confirmed the predicted geometry. From a spectroscopic standpoint, c-SiC_3 behaves as a near-prolate asymmetric rotor with an asymmetry parameter $\kappa = -0.945$, indicative of its slightly distorted, nonsymmetric prolate configuration. The molecule possesses a substantial permanent electric dipole moment of approximately 4.2 D (Alberts et al. 1990), oriented along its principal a-axis, which facilitates the observation of strong rotational transitions in both laboratory and astronomical environments. Due to the presence of two equivalent off-axis ^{12}C nuclei, the rotational spectrum is subject to nuclear spin statistics, which restrict the allowed transitions to those where the k_a quantum number, the projection of the total angular momentum along the molecular symmetry axis, only takes even integer values. This leads to distinctive rotational substructures ("k_a-stacks"), with transitions confined within and between these stacks, depending on selection rules and collisional dynamics. Indeed, because of the molecular symmetry and dipole selection rules, radiative transitions are only allowed within the same k_a-stack. As a result, radiative inter-k_a (cross-ladder) transitions are forbidden, meaning that populations cannot efficiently transfer between different k_a-stacks through spontaneous emission. However, collisional processes can drive inter-k_a transitions, since collisions are not restricted by the same selection rules. In the circumstellar envelope, collisions with the dominant partners (i.e., H_2 and also He) can transfer rotational population both within and across the k_a-stacks, controlling the excitation balance. Therefore, while radiative decay governs the excitation within a given k_a-ladder, collisions with H_2 and He are responsible for redistributing populations between ladders, linking the cross-ladder rotational temperature more directly to the kinetic temperature of the gas.

Apponi et al. (1999) precisely determined the rotational constants of c-SiC_3 using rotational spectroscopy, obtaining $A = 0.20958\,cm^{-1}$, $B = 0.17969\,cm^{-1}$, and $C = 1.26567\,cm^{-1}$. They also reported the first-order centrifugal distortion constants as $D_J = 5.56 \times 10^{-8}\,cm^{-1}$, $D_{JK} = 2.85 \times 10^{-7}\,cm^{-1}$, and $D_K = 0.0\,cm^{-1}$. These values clearly establish c-SiC_3 as an asymmetric top rotor. Accordingly, its rotational energy can be described by the effective Hamiltonian for an asymmetric top, given by

$$H_{\rm rot} = A j_x^2 + B j_y^2 + C j_z^2 - D_J j^4 - D_{JK} j^2 j_z^2 - D_K j_z^4. \quad (1)$$

The total angular momentum, j, of c-SiC_3 is related to its Cartesian components $\left(j_x, j_y, j_z\right)$ via

$$j^2 = j_x^2 + j_y^2 + j_z^2. \quad (2)$$

The rotational energy levels of c-SiC_3 are characterized by wave functions, $|j, \tau, m\rangle$, which are defined by the quantum numbers j, τ, and m. These wave functions are constructed as a linear combination of the symmetric top rotational wave functions, $|j, k, m\rangle$ (Townes & Schawlow 2013), described by

$$|j\tau m\rangle = \sum_{k=-j}^{j} a_{\tau,k}^{j} |jkm\rangle. \quad (3)$$

Here, k represents the projection of the total angular momentum j along the body-fixed a-axis, and m represents the projection of j along the space-fixed Z-axis.

Asymmetric top molecules, due to their distinct principal moments of inertia, exhibit intricate and nondegenerate rotational energy level structures. These energy levels are uniquely designated by three quantum numbers: j, k_a, and k_c. While j is the true quantum number for the total rotational angular momentum, k_a and k_c are pseudo-quantum numbers. They represent the projection of the rotational angular momentum j onto the principal inertial axis 'a' (prolate limit) and 'c' (oblate limit), respectively, in the corresponding symmetric top approximations. The index τ (where $\tau = k_a - k_c$) serves as a convenient and common label to distinguish the $2j + 1$ energy levels for a given j value, ordered by increasing energy. This indexing scheme is crucial for characterizing the specific rotational states and understanding the molecular orientation and dynamics in the absence of exact angular momentum projections along the body-fixed axes for asymmetric tops.

Due to its compact structure, c-SiC_3 exhibits small rotational constants, leading to a high density of rotational energy levels, particularly in the lower energy regions. These low-lying rotational energy levels, depicted in Fig. 1, were determined by applying the given $H_{\rm rot}$ Hamiltonian and utilizing the rotational constants reported by Apponi et al. (1999).

3. Interaction potential for the c-SiC_3–He Van der Waals complex

Our investigation involved supermolecular electronic structure computations to generate a 3D-PES for the c-$SiC_3\left(X^1A_1\right)$ +

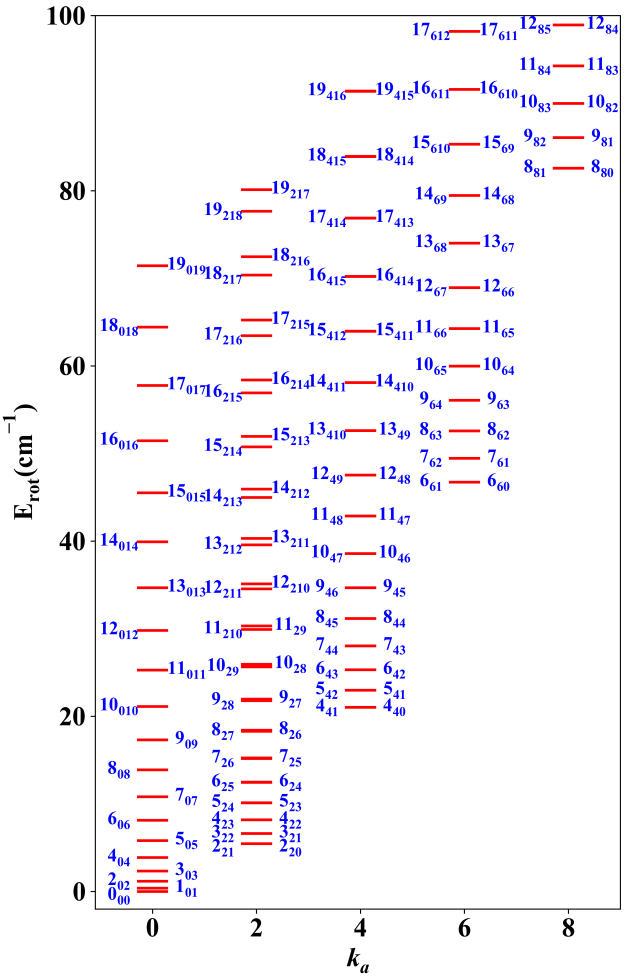

Fig. 1. Rotational energy levels of c-SiC_3 up to $j_{k_a k_c} = 12_{85}$ $\left(E_{\rm rot} = 98.9\,{\rm cm}^{-1}\right)$.

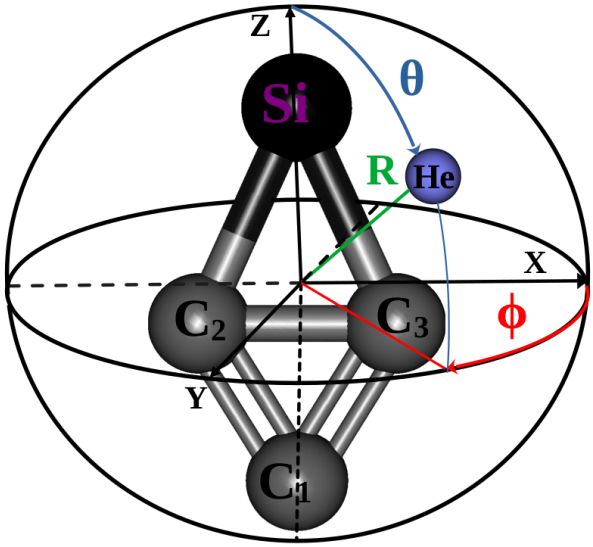

Fig. 2. Jacobi coordinate representation (R, θ, ϕ) for describing the c-SiC_3 + He van der Waals system. The origin is set at the center of mass of c-SiC_3, with the molecule lying in the XZ plane, and the planar configuration corresponding to $\phi = 0°$.

He $\left(^1{\rm S}\right)$ van der Waals complex. This mapping was performed using the Jacobi coordinate system, defined by the (R, θ, ϕ) parameters. In this system, the origin is fixed at the center of mass of the c-SiC_3 molecule, which is treated as a rigid rotor. The vector $\boldsymbol{R}$ quantifies the separation between the helium atom and the c-SiC_3 center of mass, with its magnitude, R, representing the intermolecular distance. The spatial orientation of $\boldsymbol{R}$ relative to the principal axes of inertia of c-SiC_3 is described by the two angles: θ (the polar angle), which defines the angle between $\boldsymbol{R}$ and a chosen principal axis, and ϕ (the azimuthal angle), which describes the rotation about that same principal axis.

The rigid rotor approximation is a valid assumption for the c-SiC_3 $\left(\tilde{\rm X}^1{\rm A}_1\right)$ + He $\left(^1{\rm S}\right)$ system, particularly when investigating pure rotational excitations. Previous research (Faure et al. 2005; Stoecklin et al. 2013, 2019) consistently shows that including intramonomer nuclear motions has a negligible impact on such cross-sections. While exceptions exist for highly flexible molecules like C_3 $\left(\tilde{\rm X}^1\Sigma^+\right)$ (Al Mogren et al. 2014), c-SiC_3 does not exhibit this behavior due to its high ionic character, so we would expect any such impacts to be insignificant. Therefore, when studying rotational excitations induced by He collisions, the vibrational dependence can be safely neglected at low kinetic energies. Consequently, the intramolecular geometrical parameters of c-SiC_3 were fixed at their ground-state $\left(\tilde{\rm X}^1{\rm A}_1\right)$ experimental equilibrium values (Apponi et al. 1999). This is particularly valid for energies below the threshold required to excite the first vibrational mode of c-SiC_3, which has been calculated to be 427 $\rm cm^{-1}$ using the CCSD(T)/cc-pVQZ level of theory (Linguerri et al. 2006).

Our PES computations utilized the explicitly correlated coupled-cluster method, specifically including single, double, and noniterative triple excitations, denoted as CCSD(T)-F12 (Knizia et al. 2009). For these calculations, the aug-cc-pVTZ basis set (Dunning 1989; Kendall et al. 1992) and its corresponding density fitting (DF) basis sets (Yousaf & Peterson 2008) were employed to describe the silicon, carbon, and helium atoms. All calculations were performed using the MOLPRO 2021 ab initio code (Werner et al. 2020). To accurately determine the rigid interaction potential, V, for the c-SiC_3 + He van der Waals system, we generated a 3D-PES. A crucial step in this process was applying the counterpoise correction to mitigate the basis set superposition error (BSSE) (Boys & Bernardi 1970). Consequently, the potential $V(R, \theta, \phi)$ is precisely defined as the difference between the total electronic energy of the c-SiC_3+ He complex and the sum of the electronic energies of its isolated components, as shown in Eq. (4). Critically, all energies were computed using the identical basis set employed for the complex,

$$V(R, \theta, \phi) = E_{\rm Mol+He}(R, \theta, \phi) - E_{\rm Mol}(R, \theta, \phi) - E_{\rm He}(R, \theta, \phi). \quad (4)$$

The c-SiC_3 + He interaction potential, $V(R, \theta, \phi)$, was calculated using the CCSD(T)-F12a/aug-cc-pVTZ level of theory. This theoretical approach is widely established given its accuracy in describing intermolecular interactions (Knizia et al. 2009), which has also been demonstrated in prior studies involving carbon chains interacting with He (Lique et al. 2010; Hendaoui & Mehnen 2025; Mehnen & Hendaoui 2025).

To further validate the accuracy of this computational methodology for the case of the c-SiC_3 + He complex, we evaluated the interaction potential for selected orientations corresponding to stationary points on the interaction PES. These calculations were performed using both CCSD(T)-F12a/aug-cc-pVTZ and CCSD(T)/CBS(aug-cc-pVXZ; X = T, Q, 5) approaches. For the standard CCSD(T) calculations

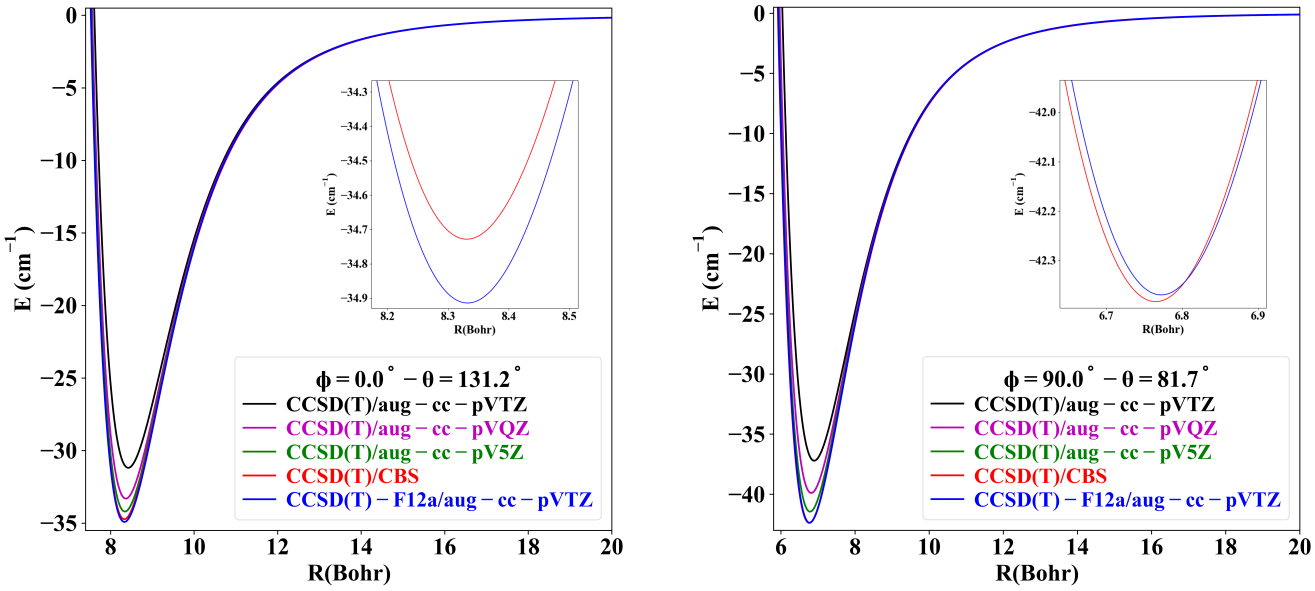

(a) (b)

Fig. 3. Radial cuts of the 3D-PES for the c-SiC_3 + He system, computed at the CCSD(T)-F12a/aug-cc-pVTZ and CCSD(T)/CBS(aug-cc-pVXZ; X=T, Q, 5) levels for the orientations $(\theta, \phi) = (131.2°, 0°)$ (a), $(81.7°, 90°)$ (b).

(Hampel et al. 1992), the interaction energies obtained with the aug-cc-pVXZ (X = T, Q, 5) basis sets were extrapolated to the complete basis set (CBS) limit using the following three-parameter scheme (Peterson et al. 1994), expressed as

$$E_x = E_{\rm CBS} + A{\rm e}^{-(X-1)} + B{\rm e}^{-(X-1)^2}, \quad (5)$$

where X represents the cardinal number of the basis set, while A, B, and $E_{\rm CBS}$ are the fitting parameters. As illustrated in Fig. 3, the potential well depth exhibits a strong dependence on the basis set size. Notably, the interaction potential energy curves obtained at the CCSD(T)-F12a/aug-cc-pVTZ level are in excellent agreement with the CCSD(T)/CBS(T, Q, 5) results, with a maximum deviation at the minimum that does not exceed 0.2 cm^{-1}. These results demonstrate that CCSD(T)-F12a/aug-cc-pVTZ achieves an accuracy comparable to that of conventional CCSD(T)/CBS extrapolation schemes, while substantially reducing the computational cost, yielding savings of at least two orders of magnitude in CPU time and disk space.

Furthermore, the benchmarks set by Lique et al. (2010) for C_4 + He, Mehnen & Hendaoui (2025) for c-SiC_2 + He and by Mehnen et al. (2026a) for C_4H + He demonstrated that the CCSD(T)-F12a/aug-cc-pVTZ method serves as a computationally efficient alternative to standard CCSD(T) calculations extrapolated to the CBS limit. This method maintains high accuracy in characterizing the interaction potential of weakly bound systems, while substantially reducing computational costs. Moreover, the benchmarks set by Mehnen & Hendaoui (2025) show that this method provides a highly accurate long-range interaction potential compared to that obtained using symmetry-adapted perturbation theory (SAPT) methods, which are widely recognized for their accurate description of long-range intermolecular interactions (Derbali et al. 2023).

4. Description of the 3D-PESs

For a precise determination of the anisotropic 3D-PES of the c-SiC_3 + He van der Waals complex, we computed a comprehensive dataset comprising 9690 energy points at the CCSD(T)-F12a/aug-cc-pVTZ level of theory. These points span a wide range of Jacobi coordinates: 51 intermolecular distances (R), ranging from 4.0 to 50.0 Bohr. 19 polar angular values (θ), from 0° to 180° in 10° increments. Ten azimuthal angular values (ϕ), from 0° to 90°. The 3D-PES of the c-SiC_3 + He van der Waals complex exhibits a pronounced anisotropy with respect to the Jacobi coordinates R, θ, and ϕ. Contour plots presented in Figs. 4a and 4b illustrate the dependence of the interaction energy on the radial distance, R, and the in-plane angle, θ, for fixed out-of-plane angles ϕ = 0 and 90°. Complementary 2D contour plots in Figs. 4c and 4d, presented for a fixed radial distances of R = 6.74 and 8.31 Bohr, further emphasize the significant anisotropic nature of this 3D-PES with respect to the angular Jacobi coordinates θ and ϕ. The global minimum (GM) of the 3D-PES is found at R = 6.74 Bohr, θ = 81.7°, and ϕ = 90°, where the helium atom lies perpendicularly above the molecular plane of c-SiC_3, corresponding to a well depth (D_e) of 42.33 cm^{-1}. When the He atom is coplanar with the c-SiC_3 molecule, two local minima (LM_1 and LM_2) and a transition state (TS_1) are identified. These correspond to the local minima and the local maximum, respectively, in the $V(R, \theta)$ 2D-PES cut shown in Fig. 4a for a fixed ϕ = 0°, where LM_1 appears at R = 8.15 Bohr and θ = 65.0° with an interaction energy of −23.2 cm^{-1}, while LM_2 occurs at R = 8.31 Bohr and θ = 131.2°, featuring a slightly deeper well of −34.9 cm^{-1}. The TS_1, located at R = 8.51 Bohr and θ = 98.0°, connects these two local minima and corresponds to an interaction energy of −19.1 cm^{-1}. The presence of multiple minima and a shallow barrier underscores the anisotropic nature of the interaction, which arises from the asymmetric electronic distribution of the cyclic c-SiC_3 molecule. These features are consistent with the behavior expected for weakly bound van der Waals complexes involving helium and cyclic molecular partners. The calculated well depth for c-SiC_3 + He (D_e = 42 cm^{-1}) is notably deeper than those reported for other similar carbon chain and metal carbide complexes with helium. For instance, the D_e for C_3 + He is 25.87 cm^{-1} (Abdallah et al. 2008); for c-MgC_2 + He, it is 20.66 cm^{-1} (M'hamdi et al. 2025); and both c-SiC_2 + He and c-CaC_2 + He exhibit a D_e of 27.39 and 25.54 cm^{-1} (Mehnen & Hendaoui 2025; Hendaoui & Mehnen

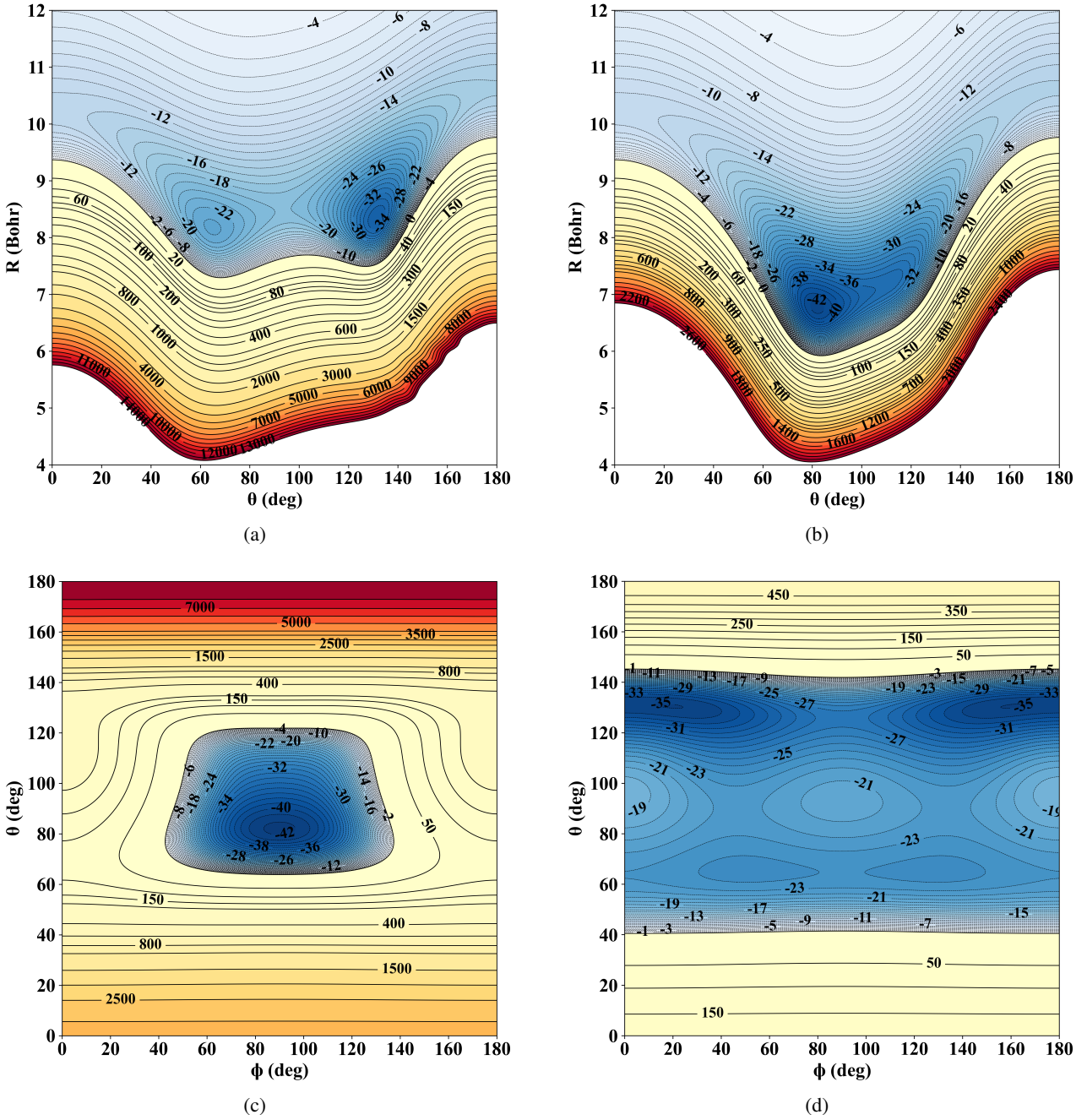

Fig. 4. 2D contour plots of the c-SiC_3 + He van der Waals 3D-PES. Top panels (a) and (b): PES as a function of radial distance (R) and in-plane angle (θ) at a fixed out-of-plane angle (ϕ) of 0 and 90 degrees. Bottom panels (c) and (d): PES as a function of θ and ϕ at a fixed intermolecular distance (R) of 6.74 and 8.31 Bohr. Blue regions indicate attractive interactions (negative potential energy in inverse centimeters), while yellow and red contours represent repulsive interactions (positive potential energy, in inverse centimeters).

2025). Conversely, longer carbon chains interacting with He, such as C_4, have shown a slightly deeper interaction potential well depth of 44.3 cm^{-1} (Lique et al. 2010). Given the significant dipole moment of c-SiC_3, reported as 4.2 D (Alberts et al. 1990), it is crucial that the interaction potential accurately represents the long-range dipole-induced interactions to ensure precise computations of low-energy cross-sections. To address this, the asymptotic behavior of the calculated PES was examined and confirmed to follow the expected $V(R) = -C_6/R^6$ dependence at large intermolecular separations. Furthermore, to validate the long-range limit of our CCSD(T)-F12 3D-PES, we performed benchmark comparisons against SAPT calculations (Derbali et al. 2023) at asymptotic intermolecular separations. The two methods demonstrated an excellent agreement across representative angular orientations.

5. Analytical representation of the 3D-PES of the c-SiC_3 + He complex

To enable the incorporation of the computed 3D-PES into subsequent scattering calculations, the corresponding ab initio data points were fitted via a least-squares procedure, yielding an analytical representation of $V(R, \theta, \phi)$. This involved expanding the potential in terms of spherical harmonics, comprised of ideal angular basis functions for describing collisions between asymmetric top molecules and atoms. Given the C_{2v} symmetry of

c-SiC_3, the expansion for $V(R,\theta,\phi)$ takes the form of Eq. (6), where $Y_l^m(\theta,\phi)$ represents the normalized spherical harmonic functions,

$$V(R,\theta,\phi) = \sum_{l=0}^{l_{\max}} \sum_{m=0}^{m_{\max}} V_{lm}(R) \frac{Y_l^m(\theta,\phi) + (-1)^m Y_l^{-m}(\theta,\phi)}{1+\delta_{m,0}}. \quad (6)$$

The $V_{lm}(R)$ radial functions correspond to the angular expansion terms and are essential for subsequent scattering calculations. The Kronecker delta, $\delta_{m,0}$, is included in the expansion. A key constraint imposed by the C_{2v} symmetry is that the quantum number m can take only even integer values. To determine the $V_{lm}(R)$ coefficients for each angular function expansion, a least-squares fitting procedure was applied at each point of the radial grid of $V(R,\theta,\phi)$. For each radial value R, the full range of m values ($0 \le m \le l$) was considered for angular momentum quantum numbers up to $l = 8$. For higher angular momentum values, specifically for $8 < l \le l_{\max}$=10, the expansion was restricted to $m_{\max} = 8$. This yielded a total of 35 angular expansion terms corresponding to the allowed (l,m) pairs. The resulting R-dependent coefficients $V_{lm}(R)$ were subsequently refined using a cubic spline interpolation procedure over the radial range $4 \le R \le 50$ Bohr, sampled at 231 points with a radial step size of 0.2 Bohr. The accuracy of this fit was rigorously ensured by minimizing the root mean square error (RMSE) value, defined in Eq. (7). This minimization process aimed to reproduce the ab initio points of the computed 3D-PES with an RMSE of less than 0.5% across all radial values. In Eq. (7), V_i^{fit} represents the fitted potential energy values, and $V_i^{\text{ab initio}}$ represents the initially computed ab initio values of the PES. Both the computed 3D-PES and its analytical form are available upon request,

$$\text{RMSE} = \sqrt{\frac{1}{N}\sum_{i=1}^{N}\left(\frac{V_i^{\text{fit}} - V_i^{\text{ab initio}}}{V_i^{\text{ab initio}}}\right)^2}. \quad (7)$$

To accurately represent the long-range interactions within the c-SiC_3 + He system, we used a long-range potential extrapolation technique. This involved an inverse exponent expansion approach, as implemented in the MOLSCAT 2022 code (Hutson & Le Sueur 2019). Furthermore, we thoroughly analyzed the long-range behavior of both the isotropic (V_{00}) and key anisotropic terms (V_{10} and V_{20}) in the interaction potential, confirming their expected asymptotic scaling. The isotropic term, $V_{00}(R)$, primarily arises from induction and dispersion interactions, exhibiting the well-known R^{-6} dependence. For the first anisotropic contribution, $V_{10}(R)$, its physical origin is linked to the interaction between the large permanent dipole moment of c-SiC_3 and the quadrupole moment induced in He (or vice versa). This interaction follows a well-established R^{-7} dependence. Similarly, $V_{20}(R)$ represents the anisotropic dipole-induced dipole interaction, which also follows an R^{-6} dependence but includes an angular component. To confirm these expected long-range behaviors for the isotropic and anisotropic terms, we analyzed scaled quantities for different $V_{lm}(R)$ components: $V_{00}(R) \times R^6 = C_6$, $V_{10}(R) \times R^7 = C_{71}$, and $V_{20}(R) \times R^6 = C_{62}$. These quantities stabilize to constant values at large distances, unequivocally confirming that each potential term adheres to its predicted power-law dependence. This validation ensures our potential model accurately captures the correct asymptotic behavior of both isotropic and anisotropic interactions. Our detailed analysis confirms that these anisotropic terms transition smoothly to their expected long-range behavior, aligning with well-established theoretical predictions and reinforcing the robustness of our interaction potential for describing inelastic rotational transition dynamics. Figure 5 illustrates the first six $V_{lm}(R)$ terms along the radial coordinate R for $l \le 4$. These terms clearly highlight the anisotropy of the c-SiC_3 + He interaction potential, as anticipated for interactions between such metal carbides and helium. Beyond the isotropic V_{00} term, which is characterized by a well depth of 49.19 cm^{-1}, the anisotropic interaction is dominated by the V_{20} term, which outweighs the V_{10} and other higher order terms. This dominance suggests a strong propensity for $\Delta j = 2$ transitions, as these are primarily driven by the V_{20} component. Accordingly, we anticipate that the resulting cross-sections and rate coefficients will follow selection rules that favor $\Delta j = 2$ transitions. This observation aligns with prior findings for metal carbides interacting with helium, such as c-SiC_2 and c-CaC_2 (Mehnen & Hendaoui 2025; Hendaoui & Mehnen 2025).

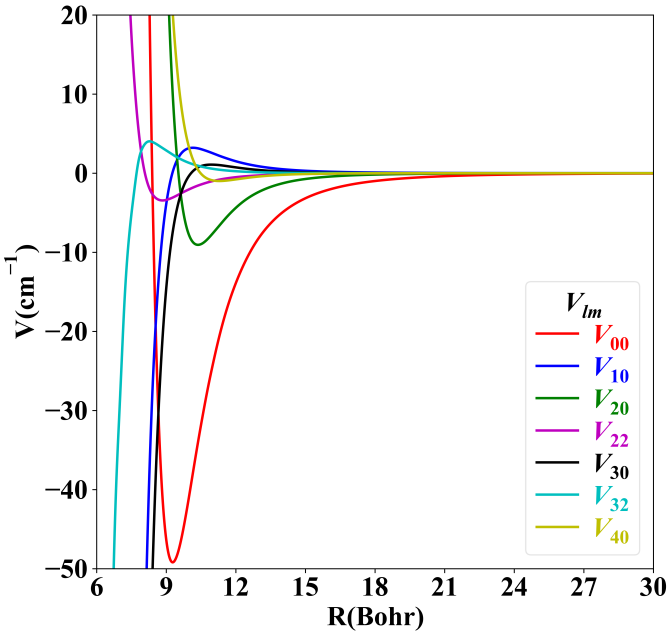

Fig. 5. $V_{lm}(R)$ terms as a function of the radial coordinate (R) for values of l up to 4.

6. Scattering calculations

Within the framework of scattering theory, we calculated the state-to-state rotational excitation and de-excitation cross-sections (σ_{if}) for c-SiC_3 molecules colliding with helium atoms. These calculations employed the time-independent close-coupling (CC) method to accurately describe the collision dynamics and the resulting transitions between initial (i) and final (f) rotational states of c-SiC_3 (Arthurs & Dalgarno 1960; Flower 2007). The computational implementation utilized the MOLSCAT program (version 2022) (Hutson & Le Sueur 2019), where we incorporated the radial components obtained from the ab initio interaction potential. The coupled-channel equations were solved using Manolopoulos (1986)'s diabatic log-derivative propagator. The reduced mass of the c-SiC_3 + He collisional system was determined to be $\mu = 3.7669$ amu. The integration of the scattering equations was performed over a meticulously optimized radial grid, spanning from $R_{\min} = 4.0$ Bohr to $R_{\max} = 40$ Bohr. To ensure both the accuracy and computational efficiency of the scattering calculations, we carefully optimized several key

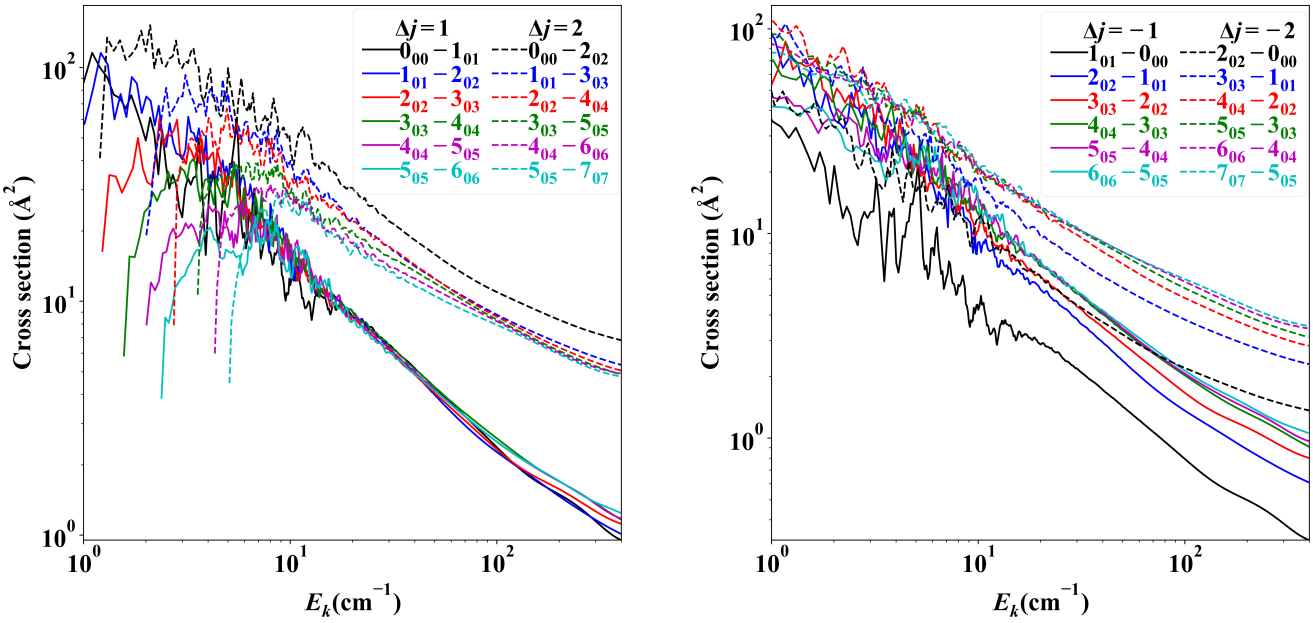

Fig. 6. State-to-state cross-sections as a function of kinetic energy (E_k) for rotational excitation (a) and de-excitation (b) of c-SiC_3 by He collisions.

parameters. The STEPS parameter, which defines the number of integration steps per half de Broglie wavelength, was adjusted according to the specific collision energy ranges. Specifically, it was set to 80, 40, and 20 steps for the energy intervals 0.1−50, 50−100, and 100−400 cm^{-1}, respectively. The convergence of the cross-sections with respect to the rotational basis set size was carefully assessed over the full energy range of 0.1 to 400 cm^{-1}. This involved systematic testing by increasing the rotational basis set size (j_{max}). We found that a basis set with $j_{max} = 19$ was able to ensure converged cross-sections for c-SiC_3 + He collisions, for transitions involving rotational levels of c-SiC_3 up to at least an internal energy of 70 cm^{-1}, covering all observed levels with a substantial margin above the highest detected states.

To meticulously capture the energy dependence of the cross-sections and identify any Feshbach or shape resonances, a dense energy grid was employed. For energies up to 200 cm^{-1}, a fine energy step of 0.1 cm^{-1} was used. For higher energies, a slightly larger step of 0.5 cm^{-1} proved sufficient. To ensure the utmost accuracy in our cross-section calculations, we utilized this high-resolution energy grid. This fine-grained approach was particularly crucial within the potential well region, where even subtle energy variations can significantly impact collision dynamics and the formation of resonances. Outside these resonant regions, where cross-section changes are less pronounced, a coarser energy grid was employed to strike a balance between computational efficiency and maintaining sufficient accuracy. Ultimately, the integral cross-section was determined by summing the contributions from individual partial waves, a method founded on the principle of conservation of total angular momentum. We confirmed the convergence of the inelastic cross-sections to within 0.005 $Å^2$ by including 81 partial waves at a total energy of 400 cm^{-1}. Figure 6 illustrates the rotational state-to-state cross-sections for both excitation and de-excitation processes ($\Delta j = \pm 1, \pm 2$) of c-SiC_3 molecule colliding with helium atoms.

At low collision energies, the cross-sections exhibit a complex and intricate resonance structure arising from a dense series of shape and Feshbach resonances associated with the formation of temporary bound states in the collision complex. As the kinetic energy (E_k) increases, these resonant features gradually diminish, and the cross-sections for both $\Delta j = \pm 1$ and ± 2 transitions evolve into a smoother, monotonically decreasing behavior. In this regime, the rotational de-excitation cross-sections are observed to decrease with increasing E_k. This behavior can be attributed to the increasing accessibility of higher rotational levels at high collision energies, which reduces the specific cross-section for transitions populating the ground rotational state ($j = 0$). For excitation, the most prominent transitions are those with $\Delta j = \Delta k_c = 2$, specifically, $0_{00} \rightarrow 2_{01}, 1_{01} \rightarrow 3_{02}$ and $2_{02} \rightarrow 4_{03}$. Conversely, for de-excitation cross-sections, $\Delta j = -2$ transitions (particularly those involving higher initial states, such as $7_{07} \rightarrow 5_{05}$, $6_{06} \rightarrow 4_{04}$, and $5_{05} \rightarrow 3_{03}$) maintain a higher magnitude than $\Delta j = -1$ transitions across both low and high collision energy regimes. For both excitation and de-excitation processes, a clear propensity trend is observed whereby the cross-sections for $\Delta j = \pm 2$ transitions consistently exceed those for $\Delta j = \pm 1$ transitions across the entire investigated energy range. This behavior is directly linked to the relative magnitudes of the anisotropic terms in the interaction potential. Specifically, although the V_{20} term is smaller in absolute magnitude than the isotropic term, it is larger than the V_{10} term in the overall potential expansion. The dominant V_{20} component effectively couples rotational levels of the same parity, thereby enhancing the $\Delta j = \pm 2$ transitions. This behavior stands in contrast to what is observed in other collision systems, such as the H_2Cl^+ + He system reported by Mehnen et al. (2024a). In that case, the anisotropic potential is dominated by the V_{10} term and where $\Delta j = \pm 1$ transitions are strongly favored, yielding significantly larger cross-sections than those for $\Delta j = \pm 2$ transitions over the explored energy range up to 10^3 cm^{-1}.

For other metal carbides, such as c-CaC_2 and c-SiC_2, in collisions with He (Hendaoui & Mehnen 2025; Mehnen & Hendaoui 2025), clear energy-dependent trends in the Δj propensities were found. These trends are governed by the varying contributions of the V_{lm} terms in the interaction potential. In particular, the V_{10} term plays a dominant role at low collision energies due

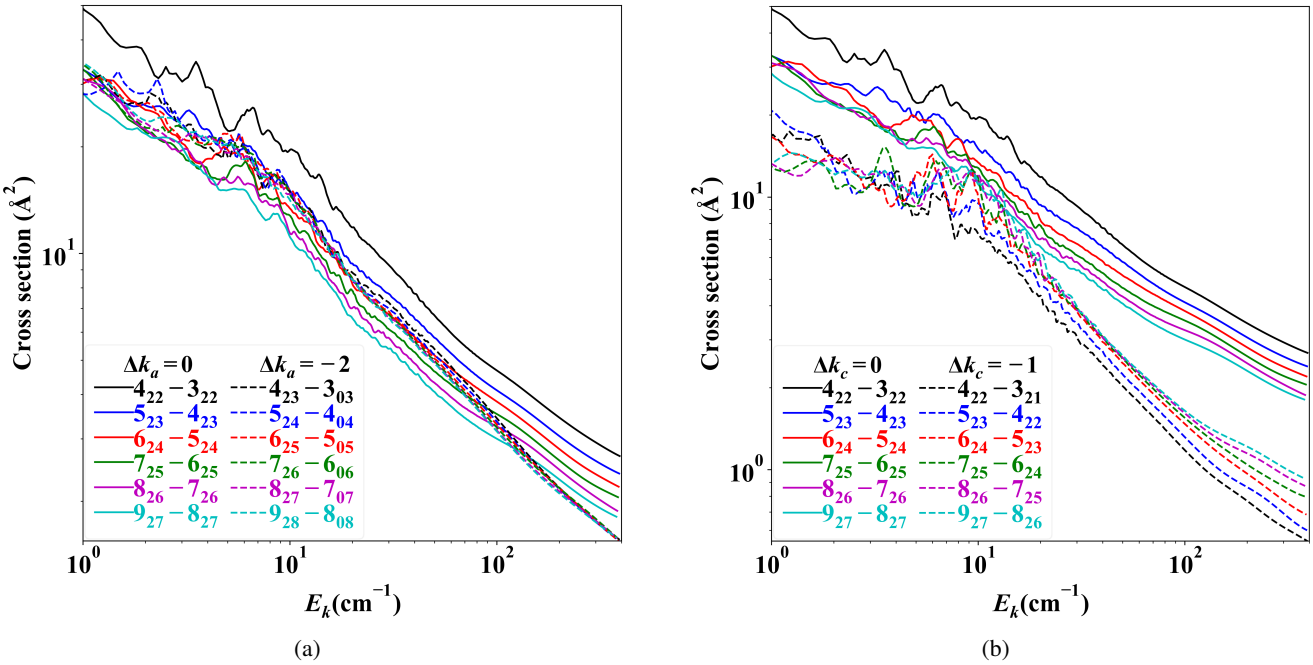

Fig. 7. State-to-state cross-sections for rotational de-excitation of c-SiC_3 by He collisions, with $\Delta j = -1$ and $\Delta k_c = 0$ with $\Delta k_a = 0$ and -2 (a), and for $\Delta j = -1$ and $\Delta k_a = 0$, while $\Delta k_c = 0, -1$ (b).

to long-range dipole interactions, favoring $\Delta j = \pm 1$ transitions, which require less energy than $\Delta j = \pm 2$ transitions. As the collision energy increases, the interaction progressively probes shorter ranges where higher order anisotropic terms become more significant. Specifically, the V_{20} component, associated with quadrupolar anisotropy, becomes more dominant and enhances $\Delta j = \pm 2$ transitions, which involve larger energy transfers. These energy-dependent Δj propensities demonstrate how both the collision energy and the relative magnitudes of the V_{lm} terms in the interaction potential govern collisional energy transfer dynamics and the resulting rotational transition selection rules, as discussed in Mehnen et al. (2024b, 2026b).

These contrasting propensities underscore the crucial role of the symmetry and anisotropy of the interaction potential in governing rotational transition probabilities. A dominant V_{20} term corresponds to a higher order anisotropic coupling favoring $\Delta j = \pm 2$ transitions, whereas a dominant V_{10} term indicates lower order coupling that enhances $\Delta j = \pm 1$ transitions. Thus, a detailed understanding of these effects reveals how the interplay between molecular structure, potential symmetry, and anisotropy fundamentally determines the collisional dynamics of molecular systems.

Figure 7 provides de-excitation cross-sections for c-SiC_3 by He collisions, illustrating how the propensity for rotational transitions is influenced by the change of k_a and k_c quantum numbers. Figure 7a depicts transitions defined by $\Delta j = -1, \Delta k_a = 0$ and -2, and $\Delta k_c = 0$, revealing that no clear propensity with respect to k_a is observed. In contrast, Fig. 7b presents the cross-sections for transitions associated with $\Delta j = -1, \Delta k_a = 0$, and $\Delta k_c = 0$ and -1, and consistently demonstrates a strong propensity based on the change of k_c. Specifically, transitions with $\Delta k_c = 0$ (solid line) maintain significantly higher cross-sections across the entire range of kinetic energies compared to those with $\Delta k_c = -1$ (dashed line). These distinct behaviors unequivocally establish the existence of propensity rules in rotational de-excitation that are critically dependent on the k_c quantum number, reflecting the complex interplay between molecular symmetry and the anisotropy of the interaction potential.

7. Rate coefficients and applications

The state-to-state cross-sections for rotational excitation and de-excitation of c-SiC_3 induced by He collisions were computed over an energy range up to 400 cm^{-1}. These cross-sections were thermally averaged over a Maxwell–Boltzmann distribution to determine the inelastic state-to-state rate coefficients, $k_{i\to f}(T)$, between initial (i) and final (f) rotational levels for temperatures up to 50 K. This is expressed as

$$k_{i\to f}(T) = \left(\frac{8}{\pi\mu\,(k_{\rm B}T)^3}\right)^{1/2} \times \int_0^{+\infty} \sigma_{i\to f} E_k e^{-\frac{E_k}{k_{\rm B}T}} dE_k, \quad (8)$$

where $k_{\rm B}$ denotes the Boltzmann constant. The resulting state-to-state rate coefficients constitute essential input for high-accuracy NLTE radiative transfer calculations, enabling a precise modeling of the molecular line intensities and rotational level populations. Consequently, these data provide a critical foundation for reliable determinations of c-SiC_3 abundances in the ISM and offer a quantitative basis for constraining the chemical pathways governing the chemistry of silicon carbides in cold astrophysical environments, including molecular clouds and circumstellar envelopes.

Figure 8 displays the excitation and de-excitation rate coefficients for $\Delta j = \pm 1$ and $\Delta j = \pm 2$ transitions, plotted against temperature up to 50 K. As Fig. 8 illustrates, the magnitude of the calculated rate coefficients is strongly dependent on the change in the rotational quantum number (Δj). For excitation rates, transitions with $\Delta j = 2$ consistently exhibit larger magnitudes than those with $\Delta j = 1$ across the entire investigated temperature range. The most prominent rates in this regime are observed for the $0_{00} \to 2_{02}$, $1_{01} \to 3_{03}$, and $2_{02} \to 4_{04}$ transitions in particular. Similarly, for de-excitation rates, $\Delta j = -2$ transitions, particularly those involving higher initial states, such as $7_{07} \to 5_{05}$ and $6_{06} \to 4_{04}$, and $5_{05} \to 3_{03}$ maintain a higher magnitude than $\Delta j = -1$ transitions up to 50 K. The sharp decrease observed in some de-excitation rate coefficients at low temperatures is attributed to threshold effects in inelastic scattering, which is fundamentally consistent with the behavior of the corresponding excitation rates via the detailed balance principle. As the

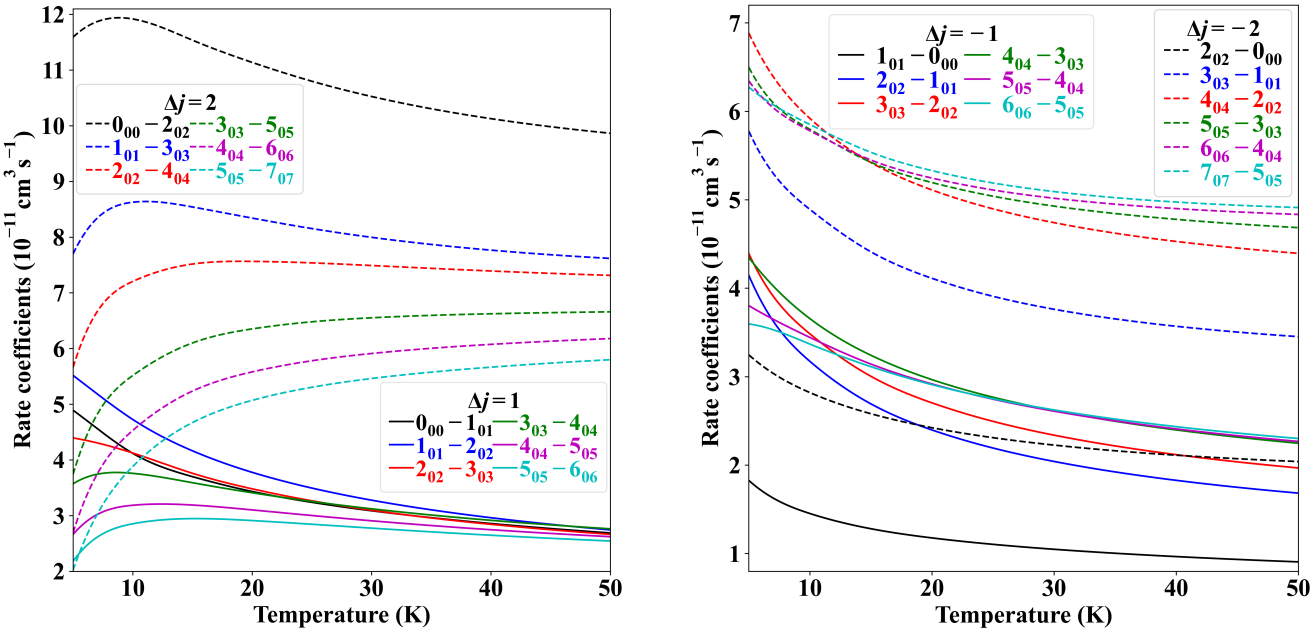

(a) (b)

Fig. 8. Temperature dependence of state-to-state rate coefficients for the rotational excitation (a) and de-excitation (b) of c-SiC_3 by He collisions.

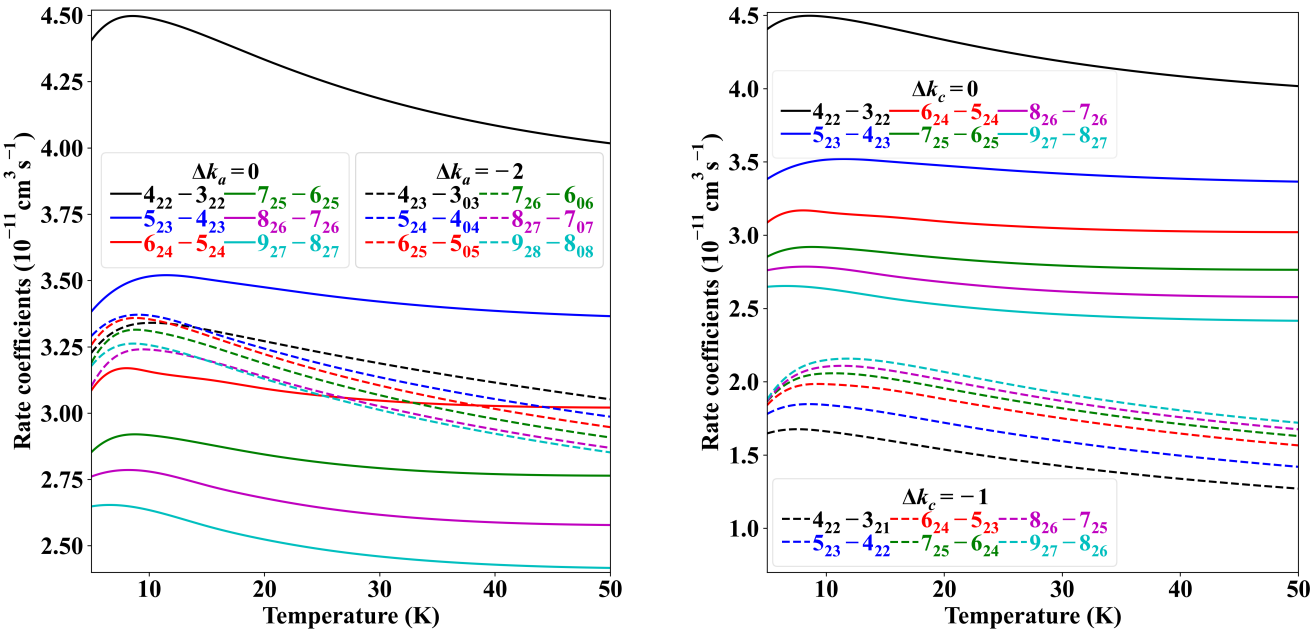

(a) (b)

Fig. 9. Temperature dependence of state-to-state rotational de-excitation rate coefficients of c-SiC_3 by He collisions, with $\Delta j = -1$ and $\Delta k_c = 0$ with $\Delta k_a = 0$ and -2 (a), and for $\Delta j = -1$ and $\Delta k_a = 0$, while $\Delta k_c = 0, -1$ (b).

collision energy approaches the transition threshold, the available phase space for both excitation and de-excitation significantly contracts, restricting the number of accessible final states. This contraction results in a substantial reduction of the corresponding cross-sections and, consequently, the rate coefficients. Furthermore, the energy gap between the initial and final states plays a critical role in dictating the thermal population redistribution dynamics.

In the observational study of rhomboidal c-SiC_3 in the carbon-rich circumstellar envelope of IRC+10216 (Apponi et al. 1999), seven distinct rotational transitions of the molecule were successfully detected in the millimeter-wave region. The detected transitions span multiple k_a-stacks ($k_a = 0, 2, 4, 6$), which are energy ladders defined by the approximately conserved projection of angular momentum onto the molecular symmetry axis. This includes both intra- and inter- k_a-stack $\Delta j = -1$ transitions, indicating a broad sampling of the molecule's rotational energy structure. Building upon previous detections of c-SiC_3 that focused on $\Delta j = -1$ spectral lines (Apponi et al. 1999), this study proposes new candidate spectral lines for c-SiC_3 detection, informed by our rate coefficient calculations.

While astronomical observations are indeed restricted to dipole-allowed radiative transitions (primarily $\Delta j = -1$), our consideration of $\Delta j = -2$ transitions concerns their collisional

role rather than their direct observability. Although $\Delta j = -2$ transitions are spectroscopically forbidden and cannot be detected as emission or absorption lines, they are highly efficient channels for energy transfer during molecular collisions. In the NLTE conditions typical of the ISM, such collisional processes play a decisive role in redistributing the populations of rotational levels. Our results show that $\Delta j = -2$ rate coefficients remain large up to 50 K and often exceed those of $\Delta j = -1$ transitions, thereby strongly influencing the excitation balance. Neglecting these "invisible" collisional pathways would therefore lead to inaccurate predictions of the level populations and, consequently, of the intensities of the observable dipole-allowed lines. For this reason, reliable astrophysical modeling requires a full radiative transfer treatment that simultaneously accounts for Einstein A coefficients, collisional rate coefficients, and the frequency coverage of available telescopes, ensuring a physically consistent interpretation of the c-SiC_3 observed spectra.

Figure 9 illustrates the de-excitation rate coefficients, providing further insights into the influence of k_a and k_c quantum numbers on transition propensities. Figure 9a depicts de-excitation rate coefficients for transitions characterized by $\Delta j = -1, \Delta k_a = 0$ and -2, and $\Delta k_c = 0$, and reveals no distinct propensity based on the change of k_a quantum number. However, Fig. 9b focuses on $\Delta j = -1$ and $\Delta k_a = 0$ transitions with varying Δk_c (i.e., $\Delta k_c = 0$ and -1), and consistently shows significantly higher rate coefficients for $\Delta k_c = 0$ transitions across the entire temperature range, compared to those with $\Delta k_c = -1$. Collectively, these observations in Fig. 9 strongly indicate the presence of specific propensity rules that are governed by the k_c quantum number, demonstrating their crucial role in shaping the de-excitation dynamics of c-SiC_3.

The collisional rate coefficients are provided for a total of 196 rotational levels, covering a wide range of rotational excitation and de-excitation. The distribution of levels as a function of the projection quantum number k_a is as follows: 20 levels for $k_a = 0$, 36 levels for $k_a = 2$, 32 levels for $k_a = 4$, 28 levels for $k_a = 6$, 24 levels for $k_a = 8$, 20 levels for $k_a = 10$, 16 levels for $k_a = 12$, 12 levels for $k_a = 14$, and 8 levels for $k_a = 16$. This coverage ensures that, even at higher k_a values, the rotational states that significantly contribute to the level populations at the considered kinetic temperatures are included, allowing for accurate and reliable radiative transfer modeling.

In low-density interstellar environments, where molecular collisions are infrequent, collisional excitation is predominantly followed by radiative decay, especially for molecules possessing a significant dipole moment like c-SiC_3. Under these conditions, the observed spectral line intensities are primarily dictated by the excitation rate coefficients, as collisional de-excitation is a rare event. Conversely, in high-density environments, where collisional interactions are frequent, collisional de-excitation can effectively compete with or even outweigh radiative decay. In such scenarios, the rotational level populations tend to approach a Boltzmann distribution, leading to LTE. Under LTE, populations are primarily governed by temperature, making detailed knowledge of individual collisional rate coefficients less crucial for interpreting spectra. Our analysis, however, underscores the paramount importance of the newly computed excitation rate coefficients for understanding interstellar conditions where NLTE effects are significant. A precise understanding of these rates is therefore essential for accurate interpretation of spectral line intensities and for reliably inferring the physical conditions prevalent in diverse astrophysical environments.

8. Summary and conclusion

We carried out the first detailed quantum scattering study of the rotational excitation and de-excitation of interstellar rhomboidal silicon tricarbide (c-SiC_3) in collisions with helium atoms, under conditions relevant to cold astrophysical environments. A highly accurate 3D-PES was computed using the CCSD(T)-F12a/aug-cc-pVTZ level of theory over an extensive grid of geometries and analytically represented through a spherical-harmonic expansion. The PES exhibits a global minimum of approximately 42 cm^{-1} at a T-shaped configuration, indicating a moderately deep and anisotropic interaction. Close-coupling quantum scattering calculations were performed for total energies up to 400 cm^{-1}. The resulting state-to-state cross-sections show pronounced resonance structures at low collision energies, which have been attributed to the transient formation of van der Waals complexes. The thermally averaged rate coefficients, computed for kinetic temperatures between 5 and 50 K, reveal a clear propensity for even Δj transitions, particularly $\Delta j = \pm 2$, reflecting the dominant V_{20} anisotropy of the interaction potential. These new rate coefficients constitute the first available collisional data for c-SiC_3 and provide essential input for NLTE radiative transfer models. They will enable a more reliable interpretation of observed millimeter-wave transitions in the carbon-rich circumstellar envelope of IRC+10216 and other similar sources.

Future works will extend the present study to include collisions of c-SiC_3 with H_2, the main collisional partners in dense molecular clouds. Such studies will be crucial for accurately modeling the excitation conditions of silicon-carbon species and for improving our understanding of the chemical and physical processes occurring in dust-forming regions around evolved stars.

Data availability

The complete set of the computed rate coefficients governing the excitation and de-excitation processes of c-SiC_3 due to inelastic collisions with He atoms will be accessible online in the BASECOL (Dubernet et al. 2013, 2024) and LAMDA (Schöier et al. 2005) databases.

Acknowledgements. B. M. acknowledges the National Science Center, Poland, for support (SONATINA 8, Grant No. 2024/52/C/ST9/00124).

References

Abdallah, D. B., Hammami, K., Najar, F., et al. 2008, ApJ, 686, 379
Al Mogren, M. M., Denis-Alpizar, O., Abdallah, D. B., et al. 2014, J. Chem. Phys., 141
Alberts, I. L., Grev, R. S., & Schaefer, H. F., III 1990, J. Chem. Phys., 93, 5046
Apponi, A. J., McCarthy, M. C., Gottlieb, C. A., & Thaddeus, P. 1999, J. Chem. Phys., 111, 3911
Arthurs, A. M., & Dalgarno, A. 1960, Proc R Soc Lond A Math Phys Sci., 256, 540
Bell, M. B., Avery, L. W., & Feldman, P. A. 1993, ApJ, 417, L37
Bernath, P. F., Hinkle, K. H., & Keady, J. J. 1989, Sci., 244, 562
Boys, S. F., & Bernardi, F. J. M. P. 1970, Mol. Phys., 19, 553
Broten, N. W., Oka, T., Avery, L. W., MacLeod, J. M., & Kroto, H. W. 1978, ApJ, 223, L105
Brown, R. D., Godfrey, P. D., Cragg, D. M., et al. 1985, ApJ, 297, 302
Brown, R. D., Cragg, D. M., Godfrey, P. D., et al. 1991, Origins Life, 21, 399
Cabezas, C., Agúndez, M., Fuentetaja, R., et al. 2022, A&A, 663, L2
Cernicharo, J., Gottlieb, C. A., Guelin, M., Thaddeus, P., & Vrtilek, J. M. 1989, ApJ, 341, L25
Cernicharo, J., McCarthy, M. C., Gottlieb, C. A., et al. 2015, ApJL, 806, L3
Cernicharo, J., Cabezas, C., Pardo, J., et al. 2019, A&A, 630, L2
Cernicharo, J., Marcelino, N., Agúndez, M., et al. 2020, A&A, 642, L8

Cernicharo, J., Cabezas, C., Agúndez, M., et al. 2021, A&A, 648, L3
Cernicharo, J., Pardo, J. R., Agúndez, M., et al. 2025, A&A, 700, L20
Derbali, E., Ajili, Y., Mehnen, B., et al. 2023, Phys. Chem. Chem. Phys., 25, 30198
Dubernet, M.-L., Alexander, M. H., Ba, Y. A., et al. 2013, A&A, 553, A50
Dubernet, M. L., Boursier, C., Denis-Alpizar, O., et al. 2024, A&A, 683, A40
Dunning, T. H., Jr 1989, J. Chem. Phys., 90, 1007
Faure, A., Valiron, P., Wernli, M., et al. 2005, J. Chem. Phys., 122
Flower, D. 2007, Molecular Collisions in the Interstellar Medium (Cambridge University Press), 42
Gottlieb, C. A., Gottlieb, E. W., Thaddeus, P., & Kawamura, H. 1983, ApJ, 275, 916
Guélin, M., Green, S., & Thaddeus, P. 1978, ApJ, 224, L27
Guélin, M., Muller, S., Cernicharo, J., et al. 2000, A&A, 363, L9
Guélin, M., Muller, S., Cernicharo, J., McCarthy, M., & Thaddeus, P. 2004, A&A, 426, L49
Hampel, C., Peterson, K. A., & Werner, H.-J. 1992, Chem. Phys. Lett., 190, 1
Hendaoui, H., & Mehnen, B. 2025, MNRAS, 539, 1180
Hinkle, K. W., Keady, J. J., & Bernath, P. F. 1988, Science, 241, 1319
Howe, D. A., & Millar, T. J. 1990, MNRAS, 244, 444
Hutson, J. M., & Le Sueur, C. R. 2019, Comput. Phys. Commun., 241, 9
Kawaguchi, K., Ohishi, M., Ishikawa, S.-I., & Kaifu, N. 1992a, ApJ, 386, L51
Kawaguchi, K., Takano, S., Ohishi, M., et al. 1992b, ApJ, 396, L49
Kawaguchi, K., Kagi, E., Hirano, T., Takano, S., & Saito, S. 1993, ApJ, 406, L39
Kendall, R. A., Dunning, T. H., Jr, & Harrison, R. J. 1992, J. Chem. Phys., 96, 6796
Knizia, G., Adler, T. B., & Werner, H.-J. 2009, J. Chem. Phys., 130
Linguerri, R., Rosmus, P., & Carter, S. 2006, J. Chem. Phys., 125
Lique, F., Kłos, J., & Hochlaf, M. 2010, Phys. Chem. Chem. Phys., 12, 15672
Loomis, R. A., Burkhardt, A. M., Shingledecker, C. N., et al. 2021, Nat. Astron., 5, 188
Mangum, J. G., & Wootten, A. 1990, A&A, 239, 319
Manolopoulos, D. E. 1986, J. Chem. Phys., 85, 6425
McCarthy, M. C., Apponi, A. J., Gottlieb, C. A., & Thaddeus, P. 2000, ApJ, 538, 766
McGuire, B. A. 2022, ApJS, 259, 30
Mehnen, B., & Hendaoui, H. 2025, MNRAS, 543, 95
Mehnen, B., Hendaoui, H., Ajili, Y., et al. 2024a, MNRAS, 529, 2753
Mehnen, B., Hendaoui, H., & Żuchowski, P. 2024b, MNRAS, 533, 1927
Mehnen, B., Hendaoui, H., Abdallah, D. B., & Hochlaf, M. 2026a, A&A, 706, A187
Mehnen, B., Hendaoui, H., Abdallah, D. B., et al. 2026b, MNRAS, 545, staf2142
M'hamdi, M., Bop, C. T., Lique, F., Ben Houria, A., & Hammami, K. 2025, MNRAS, 536, 1791
Ohishi, M., Kawaguchi, K., Kaifu, N., et al. 1991, ASP Conf. Ser., 16, 387
Pardo, J. R., Cabezas, C., Fonfría, J. P., et al. 2021, A&A, 652, L13
Pardo, J. R., Fonfría, J. P., Agúndez, M., et al. 2025, A&A, 700, L6
Peterson, K. A., Woon, D. E., & Dunning, T. H., Jr 1994, J. Chem. Phys., 100, 7410
Saito, S., Kawaguchi, K., Yamamoto, S., et al. 1987, ApJ, 317, L115
Schöier, F. L., van der Tak, F. F. S., van Dishoeck, E. F., & Black, J. H. 2005, A&A, 432, 369
Souza, S. P., & Lutz, B. L. 1977, ApJ, 216, L49
Stoecklin, T., Denis-Alpizar, O., Halvick, P., & Dubernet, M.-L. 2013, J. Chem. Phys., 139
Stoecklin, T., Denis-Alpizar, O., Clergerie, A., et al. 2019, J. Phys. Chem. A, 123, 5704
Thaddeus, P., Cummins, S. E., & Linke, R. A. 1984, ApJ, 283, L45
Thaddeus, P., Gottlieb, C. A., Hjalmarson, A., et al. 1985, ApJ, 294, L49
Townes, C. H., & Schawlow, A. L. 2013, Microwave Spectroscopy (Courier Corporation)
Tucker, K. D., Kutner, M. L., & Thaddeus, P. 1974, ApJ, 193, L115
Werner, H. J., Knowles, P. J., Manby, F. R., et al. 2020, WIREs Comput. Mol. Sci, 2, 242
Yamamoto, S., Saito, S., Kawaguchi, K., et al. 1987, ApJ, 317, L119
Yousaf, K. E., & Peterson, K. A. 2008, J. Chem. Phys., 129